SPICE

Sentinel-3 Performance improvement for ICE sheets

ATBDv2.1

Scientific Exploitation of Operational Missions (SEOM)

Sentinel-3 SAR Altimetry

Study 4: Ice Sheets

Prepared by	:	isardSAT	date:	19/04/2018
Issued by	:	isardSAT	date:	19/04/2018
Checked by	:	Malcolm McMillan	date:	19/04/2018
Approved by	:	Malcolm McMillan	date:	19/04/2018
Accepted by	:	ESA | Jérôme Benveniste	date:	19/04/2018

Contents

Table of Figures

Acronyms and Abbreviations

AD	Applicable Documents
ATBD	Algorithm Theoretical Baseline Document
ATT	ATTenuation
AW	Antenna Weighting
CAL1	CALibration type 1
CAL2	CALibration type 2
CHD	CHaracteriseD parameters file
CLS	Collecte Localisation Satellites
CNF	CoNFigured parameters file
COG	Center of Gravity
CP4O	CryoSat-2 Plus For Ocean
CST	ConSTant parameters file
DDP	Delay Doppler Processor
DEM	Digital Elevation Map
DPM	Detailed Processing Model
ESA	European Space Agency
FBR	Full Bit Rate
FFT	Fast Fourier Transform
HR	High Resolution
IODD	Input/Output Description Document
IQ	In-phase and Quadrature components of a signal
ISP	Instrument Source Packets
ITT	Invitation To Tender
KO	Kick off meeting
LEGOS	Laboratoire d’Etudes en Géophysique et Océanographie Spatiales

LRM	Low Resolution Mode
L1A	Level 1 A
L1B	Level 1 B
L1B-S	Level 1 B Stack
MPC	Mission Performance Center
OSV	Orbit State Vector
pLRM	Pseudo-LRM
PRI	Pulse Repetition Interval
PSD	Product Specification Document
PTR	Point Target Response
RB	Requirements Baseline document
RDSAR	Reduced SAR (also known as Pseudo-LRM)
RD	Reference Document
RFU	Radio Frequency Unit
SAMOSA	SAR altimetry MOde Studies and Applications
SAR	Synthetic Aperture Radar
SEOM	Scientific Exploitation of Operational Missions
SoW	Statement Of Work
SPICE	Sentinel-3 Performance improvement for Ice sheets
SR	Science Review
TCOG	Threscold Center of Gravity
TPR	Threshold Peak Retracker
TN	Technical Note
UL	University of Leeds
USO	Ultra-Stable Oscillator
WP	Work Package

Applicable Documents

Reference	Document Name	Source
AD1	Scientific Exploitation of Operational Missions (SEOM). Sentinel-3 SAR Altimetry Statement of Work (SEOM S3-4SCI SAR Altimetry). Issue 1, 27/09/2014.	ESA
AD2	Special Conditions of Tender. Appendix 4 to AO/1-8080/14/I-BG.	ESA
AD3	ESA Contract Draft. SEOM-Ice Sheets. AO/1-8080/14/I-BG.	ESA
AD4	Letter of Invitation. AO/1-8080/14/I-BG.	ESA

Table 1. Applicable Documents distributed by ESA.

Reference	Document Name	Source
UL_ESA_SEOM_S3-4SCI_CL	Cover Letter	UL
UL_ESA_SEOM_S3-4SCI_TP	Technical Proposal (v3, 2015/01/05)	UL
UL_ESA_SEOM_S3-4SCI_MP	Management Proposal (v2, 2015/01/05)	UL
UL_ESA_SEOM_S3-4SCI_IP	Implementation Proposal (v3, 2015/01/05)	UL
UL_ESA_SEOM_S3-4SCI_FP	Financial Proposal (v2, 2015/01/05)	UL
UL_ESA_SEOM_S3-4SCI_CP	Contractual Proposal (v0.1, 2015/01/05)	UL

Table 2. Proposal documents.

Reference	Document Name	Source
SPICE_ESA_SEOM_Retrackers_TN_v1.2	Retrackers Technical Note	isardSAT
UL_ESA_SEOM_SPICE_PVR	Product Validation Report	UL

Table 3. Project reference documents

1 Introduction

1.1 Purpose and Scope

This document describes the Algorithm Theoretical Basis Document (ATBD) for the Scientific Exploitation of Operational Missions (SEOM), Sentinel-3 Performance improvement for ICE sheets (SPICE) study.

The ATBD is prepared to describe the algorithms technical baseline of the processors that will be used within the project.

2 Input Files Description

For details on the input/output description of the products and the format specification of the output products for the Delay-Doppler SPICE processor please refer to SPICE deliverables IODD and PSD.

2.1 Ancillary files (CHD, CNF, CST and others)

The ancillary data can include, apart from the auxiliary files, additional information such as DEM and airborne data.

A brief description of these files follows.

<u>**Static auxiliary files:**</u>

- **Characterisation file (CHD)**: system on-ground characterization (general, time pattern, platform, antenna, calibration…)
- **Configuration file (CNF)**: contains all the Delay-Doppler or SAR processor switches and processing options that can be accordingly activated/deactivated.
- **Constants File (CST)**: includes the main physical constants used in the Level-1A to Level-2 processor.
- **Azimuth weighting file**: includes the weighting applied at burst level prior to azimuth processing.
- **DEM**: digital elevation maps (from both traditional and laser altimeters) used for validation.

3 pLRM chain

3.1 Purpose and Scope

The pLRM processor ingests the full rate complex waveforms, which are the starting point for the (SAR) high resolution processing, and aims to emulate the LRM processing on-board the satellite. This implies an average of the waveforms and a range compression. Further details of each step are described in the following sections. The L1B is then the final output of the pLRM processor. It contains geo-located and fully calibrated improved Low Resolution power echoes.

3.2 Data Block Diagram

Figure 3-1 shows the general pLRM L1 chain processing block diagram, developed for Sentinel-6 Poseidon-4 Ground Processor Prototype and adapted to CryoSat-2 for the purpose of the SPICE project. The processing steps are equivalent to those described in RD. 14.

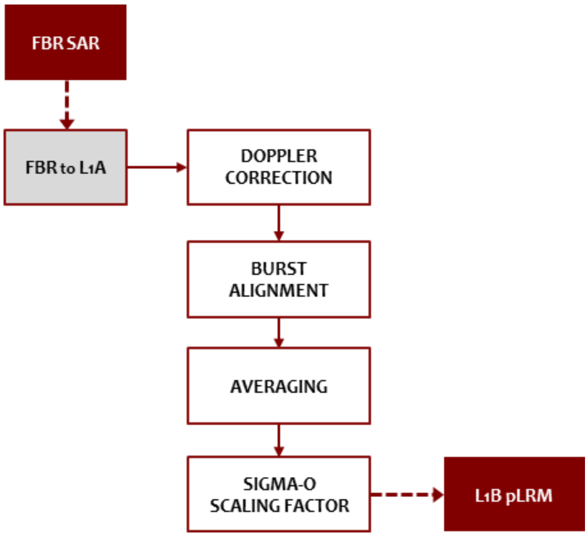

Figure 3-1. General pLRM chain block diagram

3.3 Mathematical description

3.3.1 FBR to L1A

Since both the pLRM and SAR processors in the Sentinel-6 Poseidon-4 Ground Processor Prototype start from the L1A point of view, there is the need of implementing a module that adapts the contents of the FBR (CryoSat-2 data format) to the L1A. This means applying some calibrations to the input data such as:

- Instrument gain correction
- CAL1 correction
- CAL2 correction
- USO correction

Apart from these calibrations, there is the need of aligning the pulses within a burst by shifting them with the use of the window delay and its evolution within a radar cycle. This is what is called the intra-burst alignment.

3.3.2 Doppler Correction

In the HR chain, the Doppler correction is not compensated in the L1A but to the stack data (see Azimuth Processing and Stacking). Hence, in the LR chain, it needs to be taken into account here, before the waveforms are aligned.

The Doppler correction is defined as in Eq. 3-1:

$$\Delta\tau_D(q) = -\frac{2 \cdot \dot{H}(q)}{\lambda \cdot \beta} \quad (\mathrm{s}) \qquad \text{Eq. 3-1}$$

where

$\dot{H}(q)$ is the altitude rate of each burst, being $q \in [0, N_{bc} - 1]$ the burst index and N_{bc} the number of bursts within a radar cycle.

λ is the radar wavelength,

β is the chirp slope.

After that, the Doppler correction is added to the window delay, as in Eq. 3-2

$$\tau_{wd}^{Ku}(q) = \tau_{Rx}^{Ku}(q) + \Delta\tau_D(q) \quad (s) \qquad \text{Eq. 3-2}$$

where

τ_{wd}^{Ku} is the window delay for each burst, with the Doppler correction applied to it,

τ_{Rx}^{Ku} is the window delay for each burst,

$\Delta\tau_D$ is the Doppler correction, in seconds,

$q \in [0, N_{bc}-1]$ is the burst index and N_{bc} the number of bursts within a radar cycle.

3.3.3 Burst alignment

Before computing the power waveforms that are going to be averaged, the different bursts need to be aligned. This alignment is done with respect to a reference burst within the radar cycle (the first burst) and is applied as an exponential in frequency domain, as shown in Eq. 3-3:

$$Y_{aligned}(q,p,n) = Y_{corr}(q,p,n) \cdot e^{2\pi\theta_{ib}(q)\cdot n/N_s} \qquad \text{Eq. 3-3}$$

where

$Y_{corr}(q,p,n)$ is sample *n* of L1A waveform *p* within burst *q*

$\theta_{ib}(q)$ is the inter-burst phase shift, computed as in Eq. 3-4

N_S is the number of samples of a waveform.

$$\theta_{ib}(q) = \left(\left[\tau_{wd}^{Ku}(q) - \tau_{wd}^{Ku}(q_{ref})\right] - \left[h(q) - h(q_{ref})\right]\cdot\frac{2}{c}\right)\cdot\frac{1}{T0} \qquad \text{Eq. 3-4}$$

where

$\tau_{wd}^{Ku}(q)$ is the window delay of each burst with the Doppler correction applied,

$h(q)$ is the altitude of the satellite at each burst position,

q_{ref} is the reference burst index,

$T0$ is the altimeter clock period,

c is the speed of light.

3.3.4 Averaging

Once the bursts within a radar cycle have been aligned, the power waveforms $\Psi_{aligned}$ are computed (through an FFT and a square modulus of $Y_{aligned}$, see 4.5) and then the two-step average is performed.

First, all the waveforms in each burst are averaged, as in Eq. 3-5

$$\Psi_{av}^{burst}(q,n) = \frac{1}{N_p}\sum_{p=0}^{N_p-1}\Psi_{aligned}(q,p,n) \qquad \text{Eq. 3-5}$$

where N_p is the number of pulses within a burst.

After this is done for all the bursts in a radar cycle, there is one waveform per burst. Then, the second average is performed to average all the burst waveforms in the radar cycle, as in Eq. 3-6.

$$\Psi_{av}^{RC}(n) = \frac{1}{N_{bc}}\sum_{q=0}^{N_{bc}-1}\Psi_{av}^{burst}(q,n) \qquad \text{Eq. 3-6}$$

3.3.5 Sigma-0 Scaling Factor

The sigma-0 scaling factor is computed from the averaged waveform over a radar cycle by using the same formula that is used in the main processing chains of the HR processor (see4.7). However, since the pLRM is a mixture of processing modes, some parameters in the main equation, Eq. 3-7, are taken from the LR mode and others from the HR mode. Further details are given below.

$$P_{Rx} = P_{Tx}\cdot G_{ANT_{Tx}}\frac{1}{4\pi\cdot r^2}\sigma^{o}(\theta)\cdot A_{surf}\cdot\frac{1}{4\pi\cdot r^2}\frac{\lambda^2\cdot G_{ANT_{Rx}}}{4\pi}\cdot G_{instr}\quad (\mathrm{W}) \qquad \text{Eq. 3-7}$$

In the same way it is done in HR, the sigma-0 scaling factor formula can be split in two parts: instrumental and external.

The instrumental part uses all the HR parameters its expression is defined in Eq. 3-8:

$$\kappa_i = \frac{4\pi}{P_{Tx}\cdot G_0^{\,2}\cdot\lambda^2}\quad (\mathrm{W}^{-1}\cdot\mathrm{m}^{-2}) \qquad \text{Eq. 3-8}$$

where

P_{Tx} is the power transmitted

G_0 is the transmission antenna gain for the corresponding beam

$\frac{\lambda^2\cdot G_0}{4\pi}$ is the antenna aperture amplification in reception for the corresponding beam

However, since no HR processing has been applied to the waveforms, the external contributions are inherited from the LR mode. The external factors formula is displayed in Eq. 3-9:

$$\kappa_{ext} = \frac{(16\pi \cdot B) \cdot H^3 \cdot \left(\frac{R_e + H}{\mathrm{R}_e}\right)}{c} \quad (\mathrm{m}^2) \qquad \text{Eq. 3-9}$$

where

B is the chirp bandwidth,

$\left(\frac{R_e + H}{\mathrm{R}_e}\right)$ the rounded Earth compensation, where R_e is Earth radius and H the satellite's height, and

c is the speed of light.

The final sigma-0 scaling factor is computed as in Eq. 3-10:

$$\kappa_{\sigma^0} = \kappa_i \cdot \kappa_{ext} \quad (\mathrm{W}^{-1}) \qquad \text{Eq. 3-10}$$

4 High Resolution (or SAR) Ku Chain

Figure 4-1 shows the general High Resolution (HR) Ku chain processing block diagram, developed for Sentinel-6 Poseidon-4 Ground Processor Prototype and adapted to CryoSat-2 for the purpose of the SPICE project.

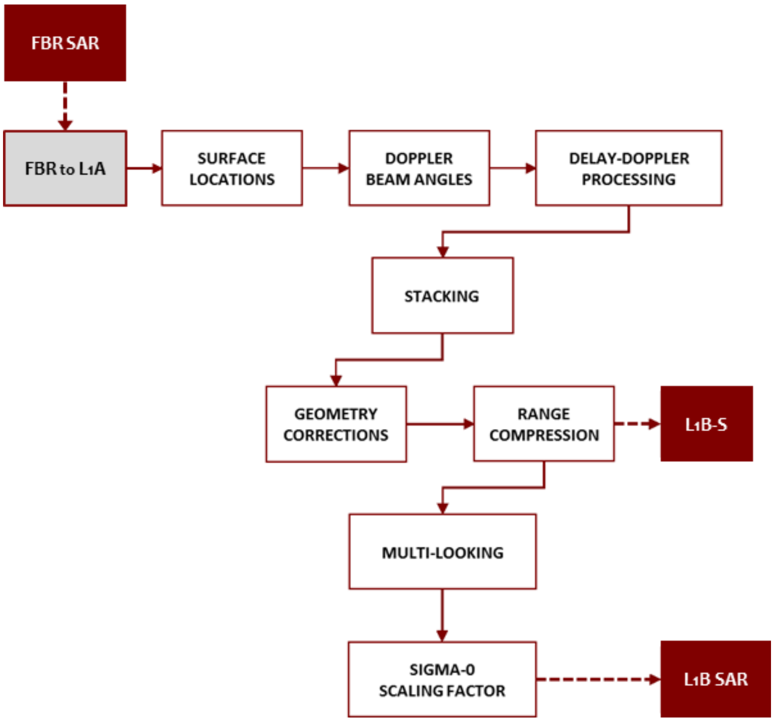

Figure 4-1. General HR (SAR) Ku chain block diagram.

The white boxes are the HR (SAR) Ku chain algorithms: Surface locations, Doppler beam angles, Delay-Doppler processing, Stacking, Geometry corrections, Range compression, Multi-looking and Sigma-0 scaling factor. The red boxes are the input, the FBR, and the output files of the chain: the L1B-S and the L1B. Each of these is described in turn.

The FBR contains geo-located bursts of Ku echoes without the calibrations applied. The FBR to L1A module (see 3.3.1) therefore applies these calibrations, to generate full rate complex waveforms, which are the starting point for the (SAR) high resolution processing. The L1B-S contains fully SAR-processed and calibrated High Resolution complex echoes, arranged in stacks after geometry corrections and prior to echo multi-look. The L1B SAR is the final output of the HR processor. It contains geo-located and fully calibrated multi-looked High Resolution power echoes. In the following sections, we describe each of the L1 processing modules.

4.1 Surface Locations, Surface Datation and Window Delay

4.1.1 Purpose and scope

The aim of this algorithm is to compute the surface locations (and their corresponding datation and orbit parameters) defined by the intersection of the Doppler beams and the estimated surface positions along the satellite track.

4.1.2 Data block diagram

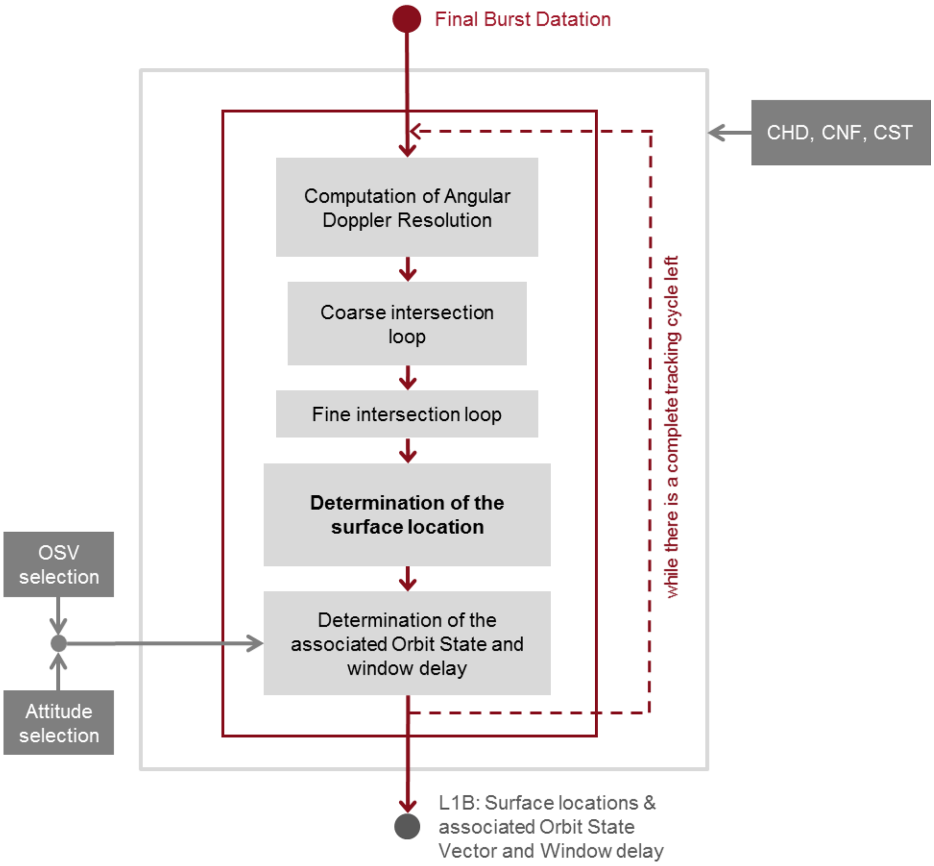

Figure 4-2. Surface Locations block diagram.

4.1.3 Mathematical description

The first surface location is determined by the window delay (time elapsed from the transmission of the pulse to the ground, and back) of the first burst of the radar cycle. Then, an iterative process starts and lasts until the end of the orbit data is reached. This process goes through the following steps:

- Computation of angular Doppler resolution

  This is obtained at the current satellite position given the Doppler frequency expression (RD. 2):

$$f_D = \frac{2\left|\vec{v}_s\right| \cdot \sin\theta}{\lambda} \quad (\text{Hz}) \qquad \text{Eq. 4-1}$$

  where $\vec{v}_s$ is the satellite velocity vector and λ the radiation wavelength. As the azimuth processing will give a Doppler frequency sampling given by the inverse of the burst duration $\left(\Delta t_{burst}\right)$, the angular azimuth beam resolution is calculated as:

$$\theta = \arcsin\left(\frac{\lambda}{2 \cdot \left|\vec{v}_s\right| \cdot \Delta t_{burst}}\right) \quad (\text{rad}) \qquad \text{Eq. 4-2}$$

- Coarse and fine intersection loops

  Determine the intersection between the direction defined by the angle θ_j (angular azimuth beam resolution, Figure 4-3) with respect to the nadir and each surface. This process is performed by iterating through the surface positions until the angle of sight (α_i)[1] is bigger than the angular azimuth beam resolution θ_j (Figure 4-4, left). Then an interpolation is performed between the last angle of sight and the previous one. After that, a second iteration process starts (the fine intersection loop) and finishes when the angle of sight coincides with the angular azimuth beam resolution (Figure 4-4, right).
- Determination of the surface location

  The new surface location (red point in Figure 4-3) is stored and used in the following step.
- Determination of the associated orbit state and window delay

  The associated orbit state can be retrieved using orbit interpolators or libraries. If not available, the orbit can be manually interpolated with splines over the burst satellite positions. Then, the new surface location is also located on the orbit (this would be the action of going from the surface to the orbit and it is represented in Figure 4-3 with the red lines going from the surface locations to the orbit). In addition, the window delay of the new surface location is calculated.

[1] A given angle of sight α_i is the angle between the nadir direction and the vector determined by the satellite position and each ground location.

- New orbit state becomes the current one and the next iteration starts.

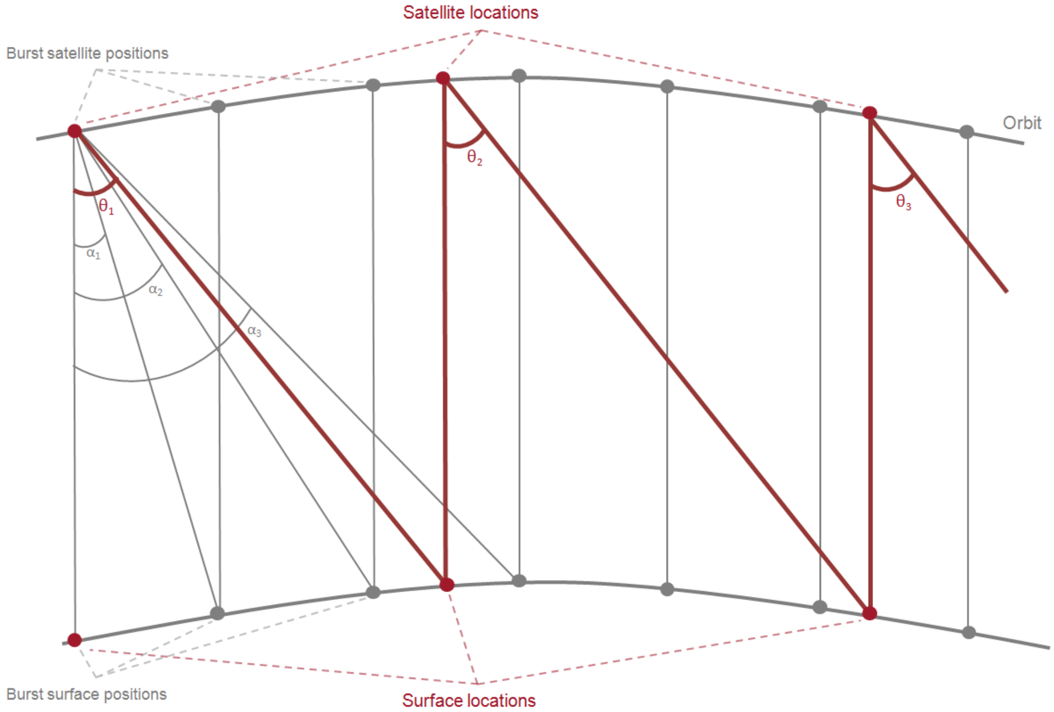

Figure 4-3. Surface Locations determination.

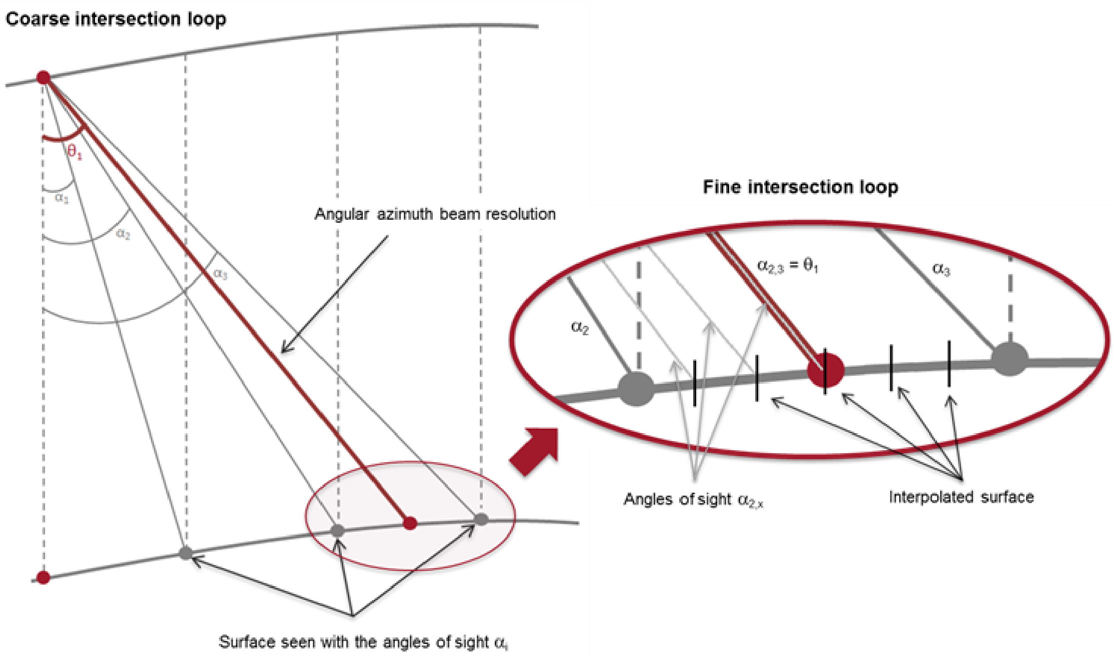

Figure 4-4. Coarse and fine intersection loops.

4.2 Beam Angles

4.2.1 Purpose and scope

This algorithm computes, for every burst, the angles between the satellite velocity vector and the direction defined by the satellite location and each surface location under the satellite's boresight.

4.2.2 Data block diagram

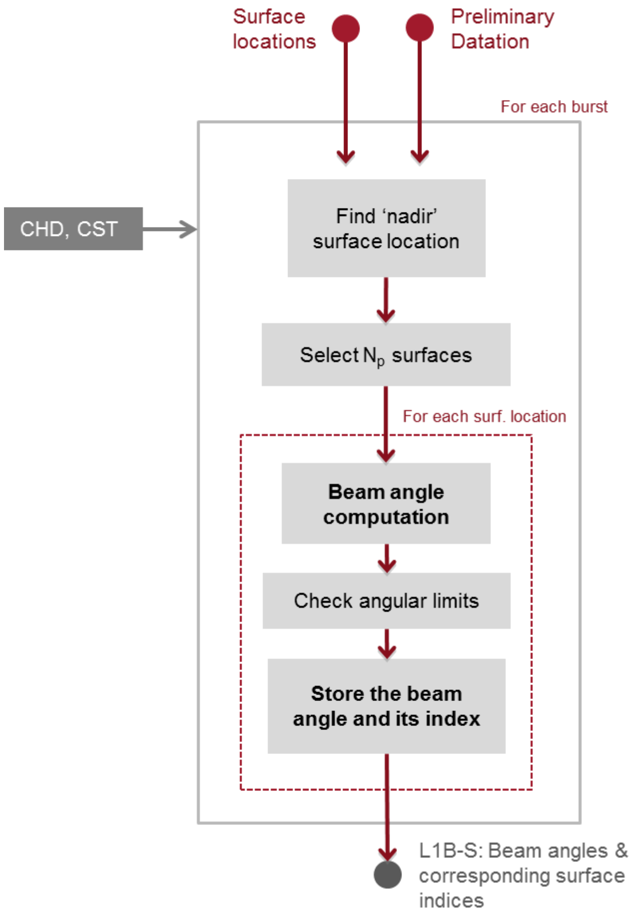

Figure 4-5. Beam Angles block diagram.

4.2.3 Mathematical description

The algorithm calculates the angles between the satellite velocity vector and the vectors connecting every surface location that is "observed" by the satellite at the current satellite burst position and the location itself. These angles are then used by the Azimuth Processing algorithm to steer the beams to the desired surface locations.

The process starts by iterating through the bursts. Then, for each burst, a few steps are followed:

- Find the surface location closest to the nadir direction and store its index.
- Select N_p surface locations: $N_p/2$ forward and $N_p/2$ backwards (see Figure 4-6).

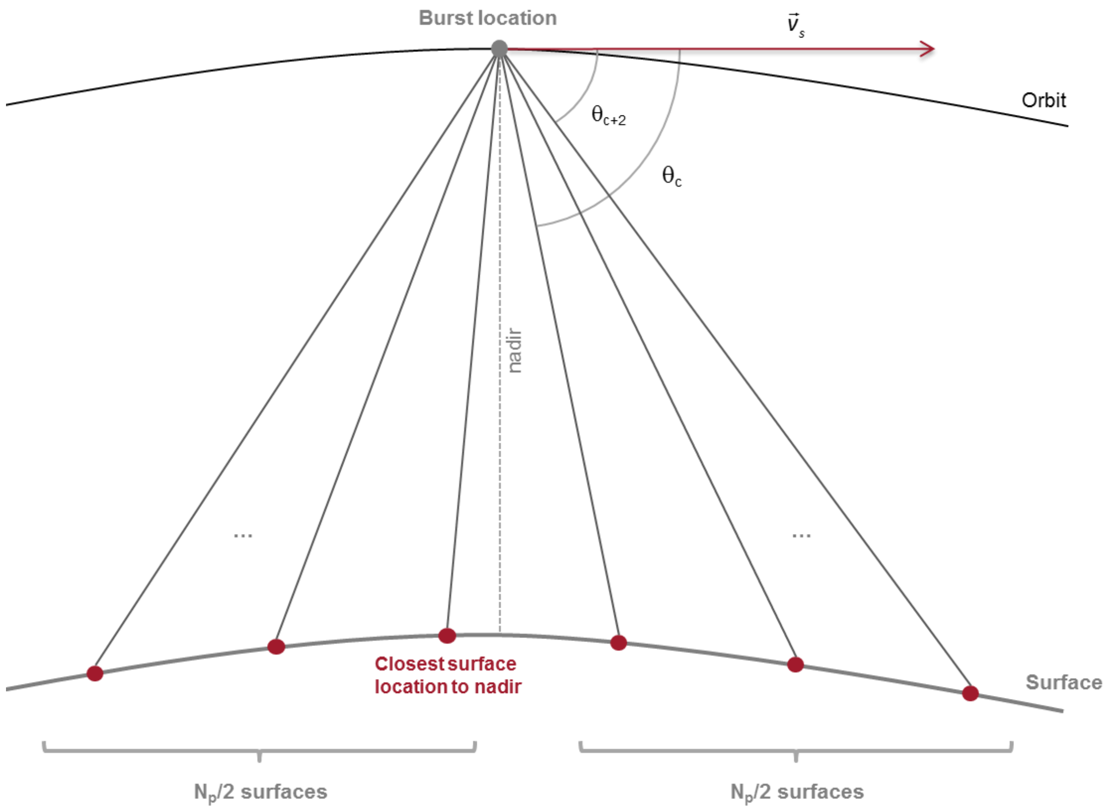

Figure 4-6. Geometry of the Beam Angles algorithm. N_p is the number of Ku pulses per burst.

- Finally, store the number of selected surface locations and their indices. These indices will be used later to generate the stack.

Then, for each surface location:

- Compute the angle between the satellite velocity vector and the satellite-to-surface direction. This angle is named beam angle and is computed the following way:

$$\theta_c = \arccos\left(\frac{\vec{V}_s \cdot \vec{W}_{sat\to surf}}{\left|\vec{V}_s\right| \cdot \left|\vec{W}_{sat\to surf}\right|}\right) \qquad \text{Eq. 4-3}$$

where $\vec{V}_s$ is the satellite velocity vector and $\vec{W}_{sat\to surf}$ is the vector from the burst satellite position to the surface location. Note that these angles, shown in Figure 4-6, are the complimentary angles of those shown in Figure 4-3and Figure 4-4.

4.3 Azimuth Processing and Stacking

4.3.1 Purpose and scope

The purposes of the azimuth processing and stacking algorithm are to steer the beams to the different surface locations and generate the stacks.

4.3.2 Data block diagram

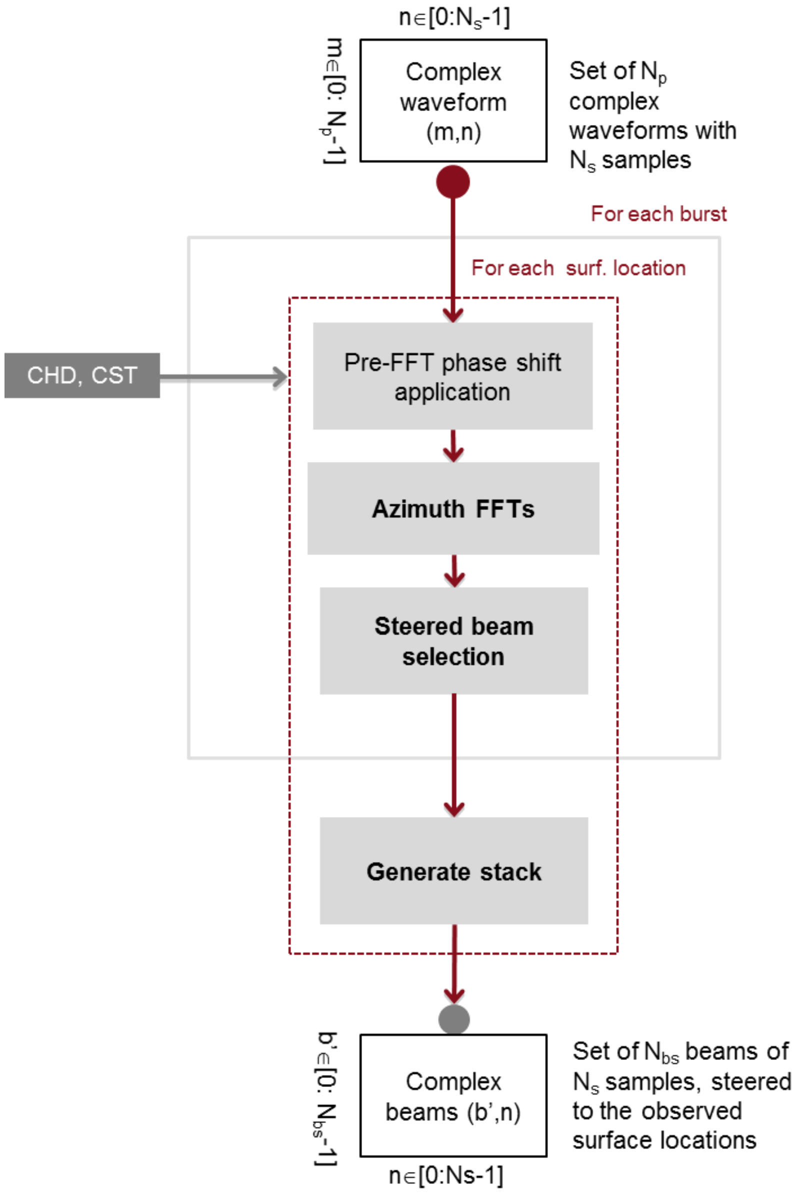

Figure 4–7. Azimuth Processing and Stacking block diagram.

4.3.3 *Mathematical description*

- Azimuth processing

In order to create Doppler beams, a specific process has to be performed in the along-track direction. This process consists in applying a different phase value to the different pulses in order to steer them towards the surface locations computed in §4.1, as originally proposed by RD. 1.

To do this, there are two different methods: the exact (see Figure 4–8), whose block diagram is depicted in Figure 4–7, and the approximate (see Figure 4–9), which is a simplification of the first.

The exact method uses all the beam angles θ_c computed in §4.2 to steer the beams to the surfaces. This implies that there will be an FFT process for each of the surface locations. On the other hand, the approximate method simply uses the beam angle that is closer to the nadir (Figure 4-6) to spread the other beams and steer them to the other surfaces. This means that the approximate method only goes through one FFT process.

Note that the FFT processes are the result of applying the steering angles θ_{beam} (or phases) to the pulses. These angles have two components:

$$\theta_{beam}(b,p) = \theta_c(b) + \delta\theta(p) = \theta_c(b) + \arcsin\left(\frac{\lambda \cdot p}{2 \cdot |\vec{V}_S| \cdot N_p \cdot PRI}\right) \quad (\text{rad}) \qquad \text{Eq. 4-4}$$

being

b the beam index within a burst, $b \in [0, N_b - 1]$

p the pulse index, $p \in \left[-\frac{N_p}{2}, \frac{N_p}{2} - 1\right]$

$\theta_c(b)$ the beam angles computed in §4.2

$\delta\theta(p)$ is the variable part, that ends up being an FFT. This second part of θ_{beam} is the one that spreads all the beams along the surface locations, being the azimuth angular beam resolution.

In order to determine which method is used, the variability of the surface (in terms of altitude) is computed using the standard deviation of the altitude of the surface locations that are seen by the current burst:

$$\sigma_{alt} = \sqrt{\frac{1}{N_b}\sum_{b=0}^{N_b-1}\left(h_{surf}(b)-\bar{h}\right)^2} \quad \text{Eq. 4-5}$$

being N_b the number of beams of the current burst, h_{surf} the altitude of each surface location and $\bar{h}$ their mean altitude. Depending on the value being above or below the pre-set threshold, the exact or approximate method will be used, respectively (see Figure 4–8 and Figure 4–9).

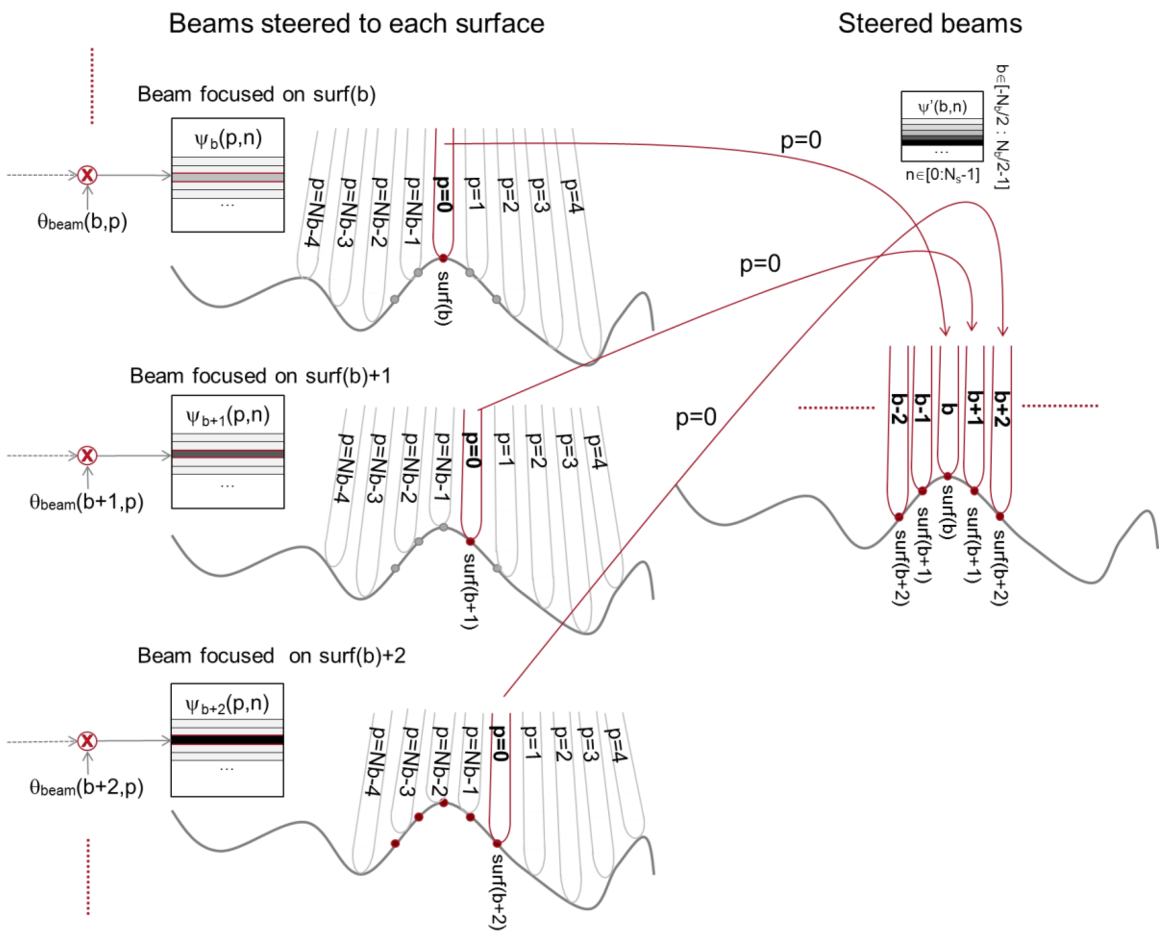

Figure 4–8. Exact beam-forming geometry. Each branch represents the process of focusing the central beam to a specific surface. ψ and ψ' represent the set of waveforms before and after the steering, respectively.

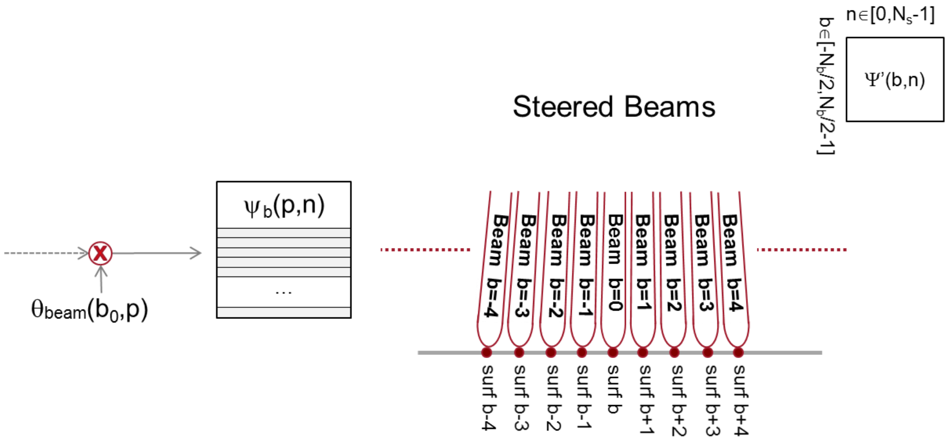

Figure 4–9. Geometry of the approximate beam-forming algorithm. Only the central beam angle b_0 is used and the other beams are equally spaced.

- Stacking

The stacking consists in gathering the beams that have illuminated each surface location. This implies changing the reference from the satellite to the surface.

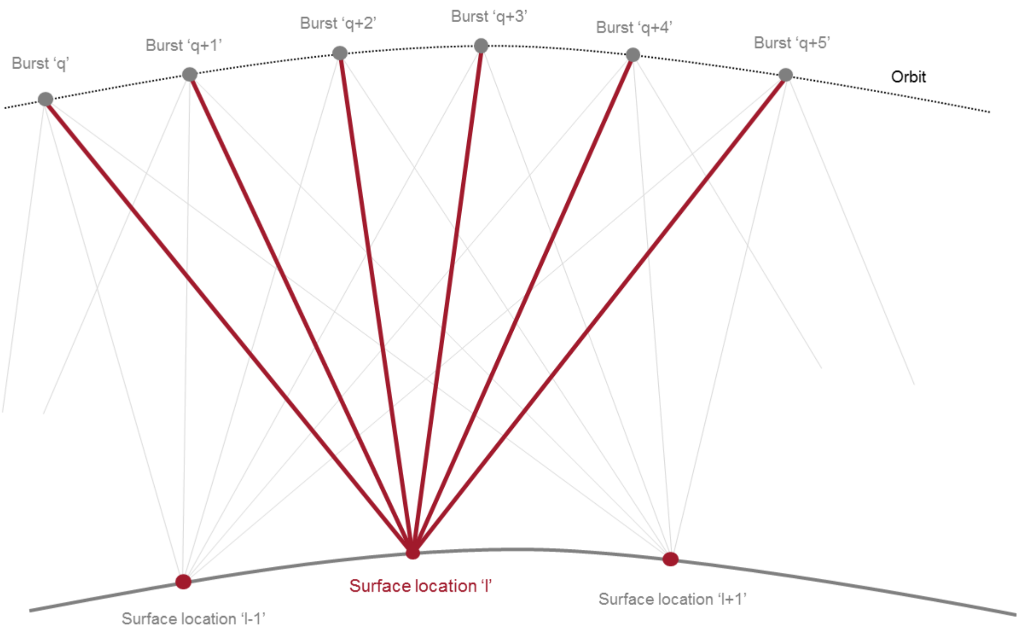

Figure 4–10. Stack formation for surface location 'l'. Red lines represent beams illuminating the surface location 'l', hence, the stack. Grey lines are other beams that have been steered to other surface locations.

4.4 Geometry Corrections

4.4.1 Purpose and scope

This section describes the following corrections:

- Doppler correction
- Slant range correction
- Window delay misalignments correction

4.4.2 Data block diagram

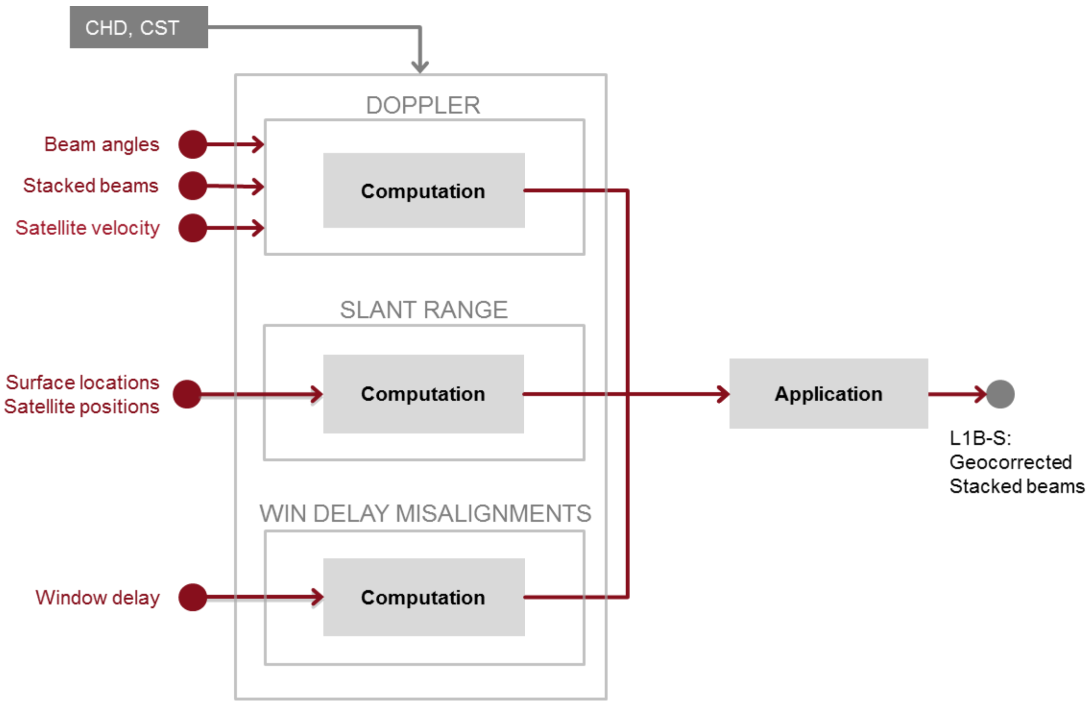

Figure 4–11. Geometry Corrections block diagram.

4.4.3 Mathematical description

This algorithm (Figure 4–11) computes and applies all the corrections associated to geometry scenarios. These are the Doppler, slant range and window delay misalignments corrections. As the stack has already been generated, the following steps are performed for each stack.

Doppler correction

The Doppler correction is needed to remove the frequency shifts due to the relative motion of the sensor and the scene. The correction is applied to the echoes in time domain, before the FFT step of the range compression.

The frequency shift for a given Doppler direction, in meters, is computed as (RD. 4):

$$\Delta r_D = -\frac{c \cdot \Delta t_{pulse}}{\lambda \cdot B} \cdot \left|\vec{v}_s(b')\right| \cdot \cos\theta_c(b') \quad (\mathrm{m}) \qquad \text{Eq. 4-6}$$

where

$\left|\vec{v}_s(b')\right|$ is the module of the satellite velocity at the corresponding satellite position,

b' is the index of beams from a stack point of view, each referring to a different burst, $b' \in [0, N_{bs} - 1]$

λ is the wavelength,

c is the speed of light,

Δt_{pulse} is the pulse length and

B is the bandwidth.

Slant range correction

This correction compensates the range migration produced by the motion of the sensor along the orbit with respect to each surface location. In Figure 4–12, the ranges of the surface location 'l', $\vec{r}(b')$ are different from the one associated to the surface location in §4.1, $\vec{h}(l)$. This difference is $\Delta r(b')$ and is computed in range as:

$$\Delta r(b') = \left|\vec{r}(b')\right| - \left|\vec{h}(l)\right| \quad (\mathrm{m}) \qquad \text{Eq. 4-7}$$

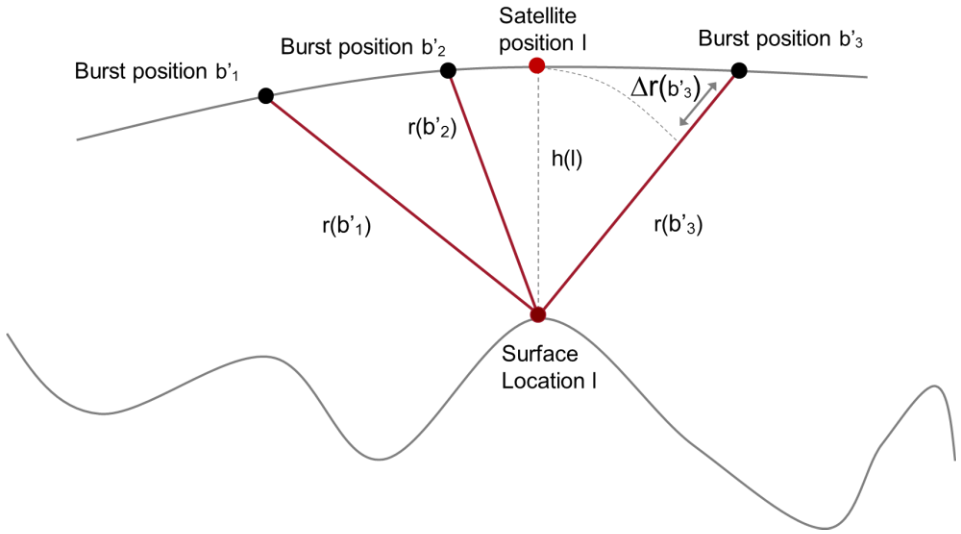

Figure 4–12. Slant range correction geometry.

Window delay misalignments

The beams of each stack come from different bursts, with different window delays. These misalignments have to be corrected. In order to do it, the window delay associated to the surface (the one computed in §4.1) is taken as a reference and the differences with all the window delays of the bursts that have built the stack are computed.

$$\Delta s_{wd}(b') = \frac{\left(\tau_{wd\,\mathrm{ref}} - \tau_{wd}(b')\right)}{T_0} \quad (\mathrm{samples}) \qquad \text{Eq. 4-8}$$

being $\tau_{wd}(b')$ the burst window delay corresponding to the b' beam, $\tau_{wd\,\mathrm{ref}}$ the reference window delay within the stack and T_0 the clock period.

These three corrections, not being an integer number of samples, are applied as a frequency shift by multiplying the beam waveforms in time by an exponential (RD. 1, RD. 2):

$$e^{j\frac{2\pi}{N_s}\cdot\Delta s(b')\cdot n} \qquad \text{Eq. 4-9}$$

being $\Delta s(b')$ the total correction in samples.

Then, the window delay associated to each surface location has to be replaced by the reference window delay within the stack.

$$\tau_{wds} = \tau_{wd\,\mathrm{ref}} \qquad \text{Eq. 4-10}$$

4.5 Range Compression

4.5.1 Purpose and scope

This algorithm (Figure 4–13) performs the transformation of the waveforms into the range domain by finalising the range compression of the input stacks and then it generates the power waveforms.

4.5.2 Data block diagram

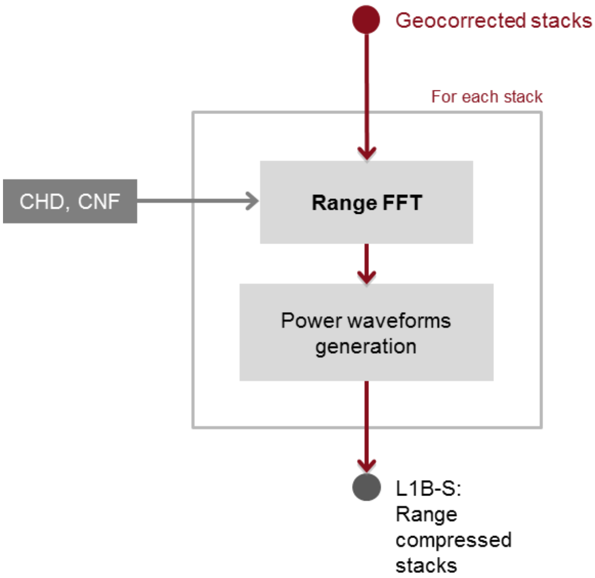

Figure 4–13. Range Compression block diagram.

4.5.3 Mathematical description

The time domain waveforms are converted into beams (frequency domain) by use of a Fast Fourier Transform (FFT), optionally with a zero-padding factor.

A zero-padding increases the number of samples of the output waveform. Thus, it provides improved results (RD. 5), as more samples are available for the geophysical fitting of the model. After that, the power waveforms for each stack Ψ_{stack} are computed.

$$\Psi_{stack}(b',n') = \left| FFT_{zp}\left\{ \psi_{gc\_stack}(b',n) \right\} \right|^2 \qquad \text{Eq. 4-11}$$

where

ψ_{gc_stack} is a stack with the geometry corrections applied

b' is the beam index within a stack, $b' \in [0, N_{bs} - 1]$, being N_{bs} the number of beams per stack

n is the sample index, $n \in [0, N_s - 1]$

n' is the zero-padded samples index, $n' \in [0,\ zp \cdot N_s - 1]$, being N_s the number of samples and zp the zero-padding factor applied in the FFT operation.

4.6 Multi-looking

4.6.1 *Purpose and scope*

The objective of this algorithm is, once the processing chain has finished, performing an average of all the waveforms that form each stack. This algorithm also computes some statistics that characterise the stack.

4.6.2 *Data block diagram*

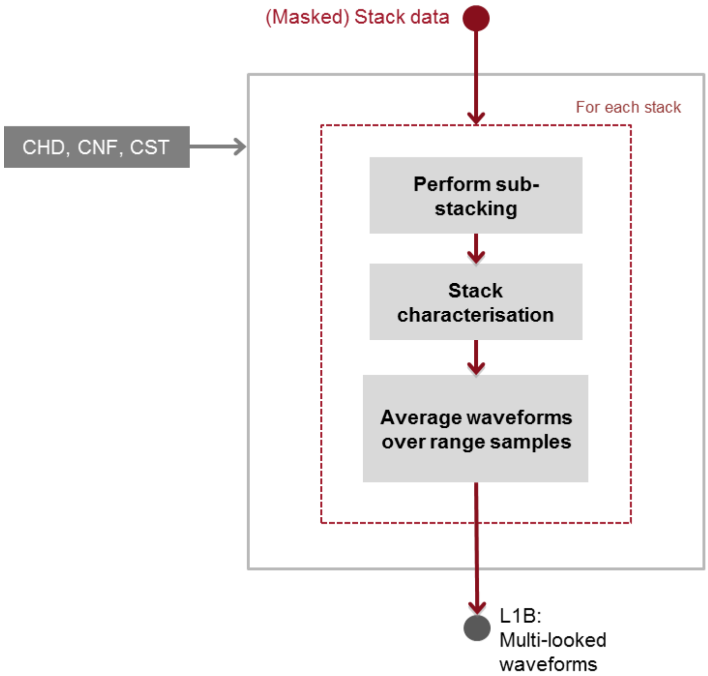

Figure 4–14. Multi-looking block diagram.

4.6.3 *Mathematical description*

The steps to multi-look the echoes in a stack into a single waveform (see Figure 4–14) are described below.

- Perform sub-stacking

  In order to compute these parameters, a sub-stacking is performed. This means grouping the total power of the beams in small groups so as to reduce the noise.

- Retrieve stack characteristics

  This reduction of the noise, leads the Gaussian fitting to a better performance. Then a few parameters that are necessary to characterise the stack (and be of use for further studies on stack data) are computed, such as 3 dB width, skewness and kurtosis.

- Weightings computation

  Before averaging the stacks, it might be of interest to remove or compensate some phenomena (i.e. the antenna weighting). These weightings can be both pre-set and/or provided by the user.

- Weighting and averaging

  After that, the weighting(s) $W(b')$ are applied and the waveforms are averaged over range samples.

$$\bar{\Psi}_{stack}(n') = \frac{1}{\sum_{b'=0}^{N_{bs}-1} W(b')} \sum_{b'=0}^{N_{bs}-1} \Psi_{stack}(b',n') \cdot W(b') \qquad \text{Eq. 4-12}$$

  Since there is still discussion on how to perform this operation in the scientific community, by the use of a configuration flag it can be done taking into account all the samples or only the non-0 ones.

4.7 Sigma-0 Scaling Factor

4.7.1 Purpose and scope

The sigma-0 scaling factor is used by Level 2 processing for computing the backscattering coefficient of the surface where the echo is reflected.

4.7.2 Data block diagram

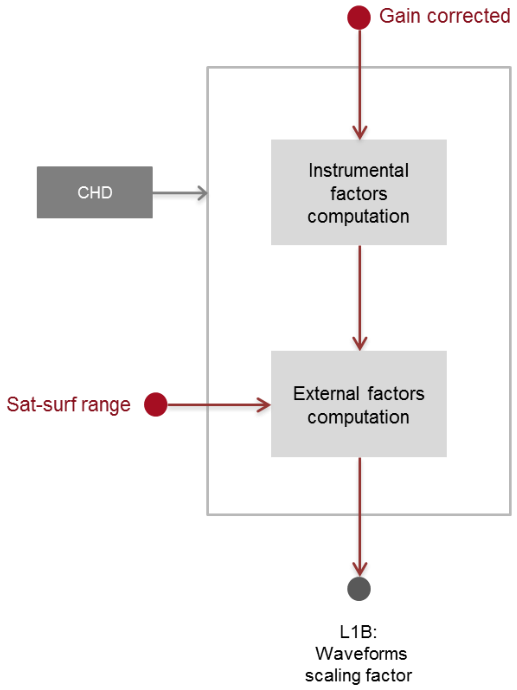

Figure 4–15. Sigma-0 Scaling Factor block diagram.

4.7.3 Mathematical description

The computation of the sigma-0 scaling factor is based on the radar equation which indicates the power relationship between the transmitted echo and the received one, considering a single beam (RD. 3).

$$P_{Rx} = P_{Tx} \cdot G_{ANT_{Tx}} \frac{1}{4\pi \cdot r^2} \sigma^0 (\theta) \cdot A_{surf} \cdot \frac{1}{4\pi \cdot r^2} \frac{\lambda^2 \cdot G_{ANT_{Rx}}}{4\pi} \cdot G_{instr} \quad \text{(W)} \qquad \text{Eq. 4-13}$$

The factors involved in the equation can be classified as instrumental and external.

The instrumental factors are:

P_{Tx} is the transmitted power

$G_{ANT_{Tx}}$ is the transmission antenna gain for the corresponding beam

$\frac{\lambda^2 \cdot G_{ANT_{Rx}}}{4\pi}$ is the antenna aperture amplification in reception for the corresponding beam

G_{instr} is the overall instrument gain.

And the external factors are:

$\frac{1}{4\pi r^2}$ is related to the attenuation due to free-space propagation[2]

$\sigma^0(\theta)$ is the backscatter coefficient. It depends on the incidence angle of the corresponding beam

A_{surf} is the area for the corresponding surface being pointed by the corresponding beam.

Then, for each beam, one sigma-0 scaling factor is computed (from the general radar equation).

$$\kappa_{\sigma^0}(b') = \frac{\sigma_o(\theta)}{P_{Rx}} = \frac{4\pi}{P_{Tx} \cdot G_0^2 \cdot \lambda^2} \cdot \frac{\left(4\pi \cdot r(b')^2\right)^2}{A_{surf}\left(r(b'), v_s(b')\right)} \quad (\mathrm{W}^{-1}) \qquad \text{Eq. 4-14}$$

Finally, the L1B sigma-0 scaling factor is obtained by averaging all the scaling factors.

$$\kappa_{\sigma^0} = \frac{1}{N_{bs}} \sum_{b'=0}^{N_{bs}-1} \kappa_{\sigma^0}(b') \quad \left(\mathrm{W}^{-1}\right) \qquad \text{Eq. 4-15}$$

[2] Attenuation introduced by atmospheric propagation is dealed with in L2 data processing.

5 Retracking

In order to retrieve geophysical information from the L1B waveforms, a retracking process is needed. The approach for the retracking stage, since some areas of interest present multi-peaked waveforms, is to have a pre-retracking module that filters out the undesired parts of the input waveforms so that the retracker can perform at its best. Figure 5-1 shows the block diagram of this setting:

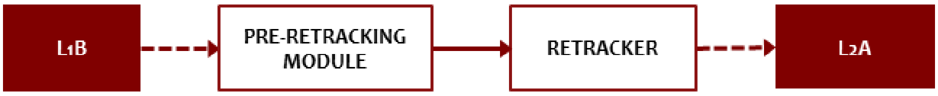

Figure 5-1. L2 chain block diagram

In this pre-retracking module, two solutions have been considered: an along-track coherence algorithm, which is also called Batch, and a waveform portion selection based on an external DEM. The option of not applying any of these is also considered. In future studies, it would be very interesting to combine both methods in order to improve the retracking performance.

Regarding the retracking itself, depending on the mode (SAR or pLRM) the best-performing retracker changes. For the purposes of this study, our primary aim is to evaluate whether an empirical or physical model based retracker performs best for SAR waveforms acquired over ice sheet surfaces. The retrackers that have been considered are an adapted ocean retracker and the best performing reference retrackers from the Phase 1 Retrackers TN (see Table 3).

5.1 Pre-retracking modules

5.1.1 Batch processing

The batch processing is based on the same concept as the along-track coherence retracker that was developed within the CP4O project[3], which monitors the window delay behaviour along the track to prevent the retracking of undesired echoes within the receiving window.

The three main steps are the following:

Avoid window delay jumps

The window delay monitoring consists in making sure its values fall within a certain moving fixed-size timespan. Depending on the scenario, this margin may change its size. Moreover, the number of records that are taken into account can also be changed. In this case, since the areas where the Batch is relevant have a rapidly changing terrain, the number records that are taken into account to set the margin is 5. Then, the current window delay is allowed to fall out of this margin up to 20 samples.

Cut the waveforms

If the new window delay is out of the margin, we search all the peaks that the waveform may have and identify the one that has been first retracked. Then, this part of the waveform is deleted.

Retrack the rebuilt waveform

The retracker is ran again, this time only with the new waveform, which does not contain the spurious signal.

This post-L1B processing can solve almost all contamination problems. Only those targets that are located very close in range to the surface echo signal could invalidate the proper range retrieval.

[3] The along-track coherence retracker was developed within the CP4O project funded by ESA (RD. 9), and partially funded by isardSAT.

This technique has been proven in coastal areas within the CP4O project with success, reducing by a 60% the along track sea level standard deviation of the coastal tracks sections with respect to ESA L2 products (RD. 9).

5.1.2 DEM-guided

This pre-retracking module makes use of an external DEM to determine which part of the waveform corresponds to the nadir direction, so as to consistently retrack the nadir surface, rather than other reflections within the beam footprint. The choice of DEM is configurable, but for the purposes of this study is chosen to be a new DEM based on 6 years of CryoSat-2 data (RD. 11) for Antarctica, and a DEM based on airborne data for the Russell Glacier (RD. 12).

The selection algorithm has the following processing logic:

<u>Check if the DEM reference is within the receiving window</u>

If the reference is not within the receiving window, a flag is raised and the algorithm exits and outputs the whole waveform sample range.

<u>Cut the waveform</u>

If the DEM reference is within the receiving window, the closest peak to this reference is selected and the waveform is cut around the valleys surrounding the selected peak[4]. When waveforms are very noisy, a smoothing is done so as to select the actual peaks instead of noise.

<u>Retrack the rebuilt waveform</u>

The retracker is ran again, this time only with the new waveform, which does not contain the spurious signal.

[4] A valley is defined here as the lowest power area between two peaks.

5.2 Retrackers

The data produced in this study utilized three retrackers, one analytical SAR retracker based on the work of Ray et al. (2015), RD. 8, and two empirical retrackers that are well established from past satellite missions. These retrackers are each described in more detail below.

5.2.1 Analytical retracker

The analytical retracker[5] (RD. 8) is based on Barrick's work on rough surface scattering based on specular point theory and considers the radar cross section as a variable value when deriving the model waveform both accounted for RD. 6 and RD. 8.

Barrick's definition under Gaussian assumption is given by:

$$\sigma(\theta) \approx \sigma_0(0)\exp\left(-\frac{\tan^2\theta}{\sigma_s}\right) \quad \text{Eq. 5-1}$$

Where θ is the incident angle, and σ_s is related to the roughness of the surface under observation.

In this way, the modelled waveform can adapt to different surface roughness conditions. Figure 5-2 shows the effect of varying σ_s from a very specular reflector ($\sigma_s = 1 \cdot e^{-6}$) to a very rough surface, $\sigma_s = 0.01$.

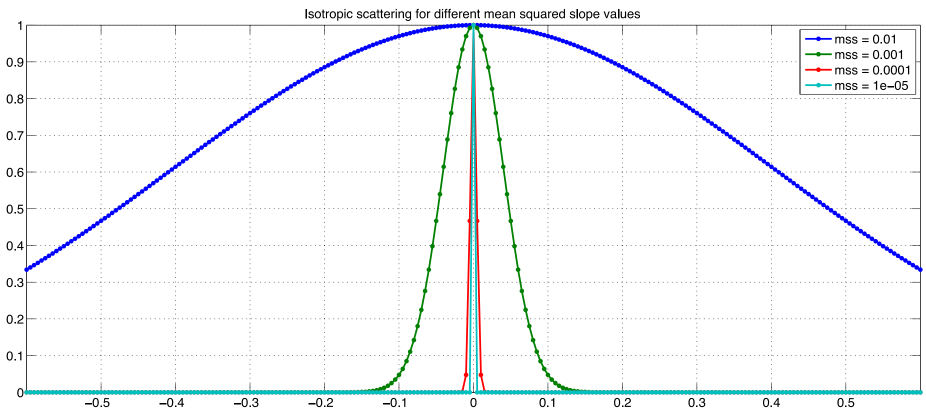

Figure 5-2. Graphical representation of Barrick's radar cross section for different σ_s.

[5] This retracker was developed within the SAMOSA project funded by ESA.

5.2.2 Threshold Peak Retracker

The Threshold Peak Retracker outputs the first sample that reaches the amplitude set by a threshold within a set range of samples $[n_1, n_2]$ that usually discards the first samples of the waveform due to high noise values. Usually this amount is $n_1 = 5$*ZP samples.

For SAR mode, the threshold has been set to 0.75·A, whereas for PLRM it has been set to 0.35·A[6], being A the maximum amplitude of the power waveform.

5.2.3 TCoG

The Threshold Centre of Gravity is a combination of the well-known COG and the TPR. Basically, the retracking point is obtained by taking the first sample that crosses the power threshold *k*·A and then linearly interpolating the echo. This *k* threshold has been set to 0.5·A.

As described in RD. 10, the algorithm is based on the following equations:

$$A = \sqrt{\frac{\sum_{i=n_1}^{n_2} P_i^4}{\sum_{i=n_1}^{n_2} P_i^2}} \quad \text{Eq. 5-2}$$

$$t_0 = i_0 - 1 + \frac{kA - P_{i_0-1}}{P_{i_0} - P_{i_0-1}} \quad \text{Eq. 5-3}$$

where i_0 is the index of the sample that first crosses the power threshold *k*·A, n_1 and n_2 the start and stop indexes (used to discard samples at the extremes of the waveform), P_i and P_{i_0} the waveform power at samples i and i_0, respectively, and t_0 the leading edge position.

The final retracking solution is TPR for SAR and TCOG for pLRM. Hence, the final percentages chosen for each mode are 75% (SAR) and 50% (pLRM).

[6] For SAR-mode ocean-like waveforms, 75% of the maximum amplitude is a rough estimation of the leading edge. For PLRM, in turn, this threshold is smaller. After a few tests, 35% was the best threshold.

6 References

RD. 1 Raney, R.K., *The Delay/Doppler radar altimeter, in Geoscience and Remote Sensing*, IEEE Transactions on Geoscience and Remote Sensing, vol.36, no.5, pp.1578-1588, Sep 1998.

RD. 2 Cumming, I.G.; Wong, F.H., *Digital Processing of Synthetic Aperture Radar Data. Algorithms and Implementation*. Boston, MA: Artech House, 2005.

RD. 3 Curlander, John C., and Robert N. McDonough. *Synthetic aperture radar*. New York, NY, USA: John Wiley & Sons, 1991.

RD. 4 Prats-Iraola, P.; Scheiber, R.; Rodriguez-Cassola, M.; Mittermayer, J.; Wollstadt, S.; De Zan, F.; Brautigam, B.; Schwerdt, M.; Reigber, A.; Moreira, A., *On the Processing of Very High Resolution Spaceborne SAR Data*, in IEEE Transactions on Geoscience and Remote Sensing, vol.52, no.10, pp.6003-6016, Oct. 2014.

RD. 5 Smith, W.H.F.; Scharroo, R., *Waveform Aliasing in Satellite Radar Altimetry*, in IEEE Transactions on Geoscience and Remote Sensing, vol.53, no.4, pp.1671-1682, April 2015.

RD. 6 Barrick Donald E. *and* Peake William H.*, (*1968*), A Review of Scattering From Surfaces With Different Roughness Scales, Radio Science, 3, doi: 10.1002/rds196838865.*

RD. 7 Fornari, M., Scagliola, M., Tagliani, N., Parrinello, T. and García-Mondéjar, A., "CryoSat: Siral calibration and performance," *Geoscience and Remote Sensing Symposium (IGARSS), 2014 IEEE International*, Quebec City, QC, 2014, pp. 702-705. doi: 10.1109/IGARSS.2014.6946520

RD. 8 Ray, C., Martin-Puig, C., Clarizia, M. P., Ruffini, G., Dinardo, S., Gommenginger, C., & Benveniste, J. (2015). *SAR altimeter backscattered waveform model.* IEEE Transactions on Geoscience and Remote Sensing*,* 53*(2), 911-919.*

RD. 9 CP4O SARin (and beyond) for Coastal Ocean. Technical Note. December 2015. isardSAT CP4O team. (http://www.satoc.eu/projects/CP4O/docs/WP1000_SARin&beyond_Coastal_TN_revised.pdf)

RD. 10 CryoVal Land-Ice project. CryoVal Land Ice Technical Note. CS2-MSSL-RTEL-0001. October 2014.

RD. 11 Slater, T., Shepherd, A., McMillan, M., Muir, A., Gilbert, L., Hogg, A., Konrad, H., Parrinello, T. (2017), A New Digital Elevation Model of Antarctica derived from 6 years of continuous CryoSat-2 observations, The Cryosphere Discussions.

RD. 12 NASA. IceBridge Data Portal. https://nsidc.org/data/icebridge/

RD. 13 ESA. Products Specification Format – CRYOSAT Ground Segment, Instrument Processing Facility L1b, ref. CS-RS-ACS-GS-5106, issue 4.9, 14th November 2011.

RD. 14 Fenoglio-Marc, L., Buchhaupt, C., 2017. TB-RDSAR for GPOD, Altimetry Coastal and Open Ocean Performance, Algorithm Theoretical Basis Document, ESA, EOEP-SEOM-EOPS-TN-17-046.